

Real-World Blind Super-Resolution via Feature Matching with Implicit High-Resolution Priors

Chaofeng Chen*
chaofenghust@gmail.com
School of Informatics,
Xiamen University
Xiamen, China

Xinyu Shi*
x98shi@uwaterloo.ca
School of Informatics,
Xiamen University
Xiamen, China

Yipeng Qin
QinY16@cardiff.ac.uk
School of Computer
Science and Informatics,
Cardiff University
Cardiff, England

Xiaoming Li
csxmli@gmail.com
Faculty of Computing,
Harbin Institute of
Technology
Harbin, China

Tao Yang
yangtao9009@gmail.com
DAMO Academy, Alibaba
Group
Shenzhen, China

Xiaoguang Han
hanxiaoguang@cuhk.edu.cn
SSE, The Chinese
University of Hong Kong
Shenzhen, China

Shihui Guo[†]
guoshihui@xmu.edu.cn
School of Informatics,
Xiamen University
Xiamen, China

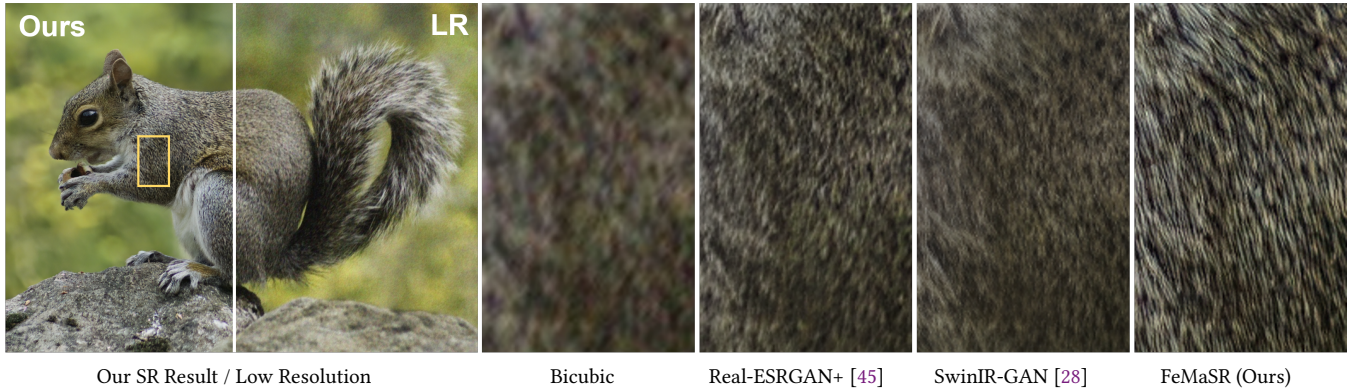


Figure 1: Comparison between our FeMaSR and two latest works, Real-ESRGAN+ [45] and SwinIR-GAN [28] on a low resolution image with complex blind degradations. Our method can recover realistic hairs for the squirrel thanks to the implicit high-resolution priors. Please zoom in for the best view.

ABSTRACT

A key challenge of real-world image super-resolution (SR) is to recover the missing details in low-resolution (LR) images with complex unknown degradations (e.g., downsampling, noise and compression). Most previous works restore such missing details in the image space. To cope with the high diversity of natural images, they either rely on the unstable GANs that are difficult to train and prone to artifacts, or resort to explicit references from high-resolution (HR)

images that are usually unavailable. In this work, we propose Feature Matching SR (FeMaSR), which restores realistic HR images in a much more compact feature space. Unlike image-space methods, our FeMaSR restores HR images by matching distorted LR image *features* to their distortion-free HR counterparts in our pretrained HR priors, and decoding the matched features to obtain realistic HR images. Specifically, our HR priors contain a discrete feature codebook and its associated decoder, which are pretrained on HR images with a Vector Quantized Generative Adversarial Network (VQGAN). Notably, we incorporate a novel semantic regularization in VQGAN to improve the quality of reconstructed images. For the feature matching, we first extract LR features with an LR encoder consisting of several Swin Transformer blocks and then follow a simple nearest neighbour strategy to match them with the pretrained codebook. In particular, we equip the LR encoder with residual shortcut connections to the decoder, which is critical to the optimization of feature matching loss and also helps to complement the possible feature matching errors. Experimental results show that our approach produces more realistic HR images than previous methods. Codes are released at <https://github.com/chaofengc/FeMaSR>.

*Both authors contributed equally to this research.

[†]Corresponding author

Permission to make digital or hard copies of all or part of this work for personal or classroom use is granted without fee provided that copies are not made or distributed for profit or commercial advantage and that copies bear this notice and the full citation on the first page. Copyrights for components of this work owned by others than ACM must be honored. Abstracting with credit is permitted. To copy otherwise, or republish, to post on servers or to redistribute to lists, requires prior specific permission and/or a fee. Request permissions from permissions.acm.org.

ACM Multimedia, October 10–14, 2022, Lisbon, Portugal

© 2022 Association for Computing Machinery.

ACM ISBN 978-1-4503-XXXX-X/18/06...\$15.00

<https://doi.org/XXXXXX.XXXXXXX>

CCS CONCEPTS

• **Computing methodologies** → **Computational photography**.

KEYWORDS

Blind Super-Resolution, FeMaSR, Feature Matching, High-Resolution Prior, VQGAN

ACM Reference Format:

Chaofeng Chen, Xinyu Shi, Yipeng Qin, Xiaoming Li, Tao Yang, Xiaoguang Han, and Shihui Guo. 2022. Real-World Blind Super-Resolution via Feature Matching with Implicit High-Resolution Priors. In *Proceedings of ACM International Conference on Multimedia (ACM Multimedia)*. ACM, New York, NY, USA, 18 pages. <https://doi.org/XXXXXXX.XXXXXXX>

1 INTRODUCTION

Single image super-resolution (SISR) is a fundamental task in low-level vision, aiming to restore high-resolution (HR) images from their low-resolution (LR) counterparts. Due to the incorporation of deep neural networks, previous works [6, 7, 28, 29, 35, 58] have made significant progress on *non-blind SR*, which assumes a known degradation process, e.g., bicubic downsampling. However, these methods usually fail in real-world SR tasks where the degradations are unknown, i.e., *blind SR*.

Blind SR is intrinsically an ill-posed problem because the complex and unknown distortions in the LR inputs have disrupted many details. Some works [13, 41, 54, 63] exploited assumptions of the classical degradation model to explicitly estimate the blur kernel and noise. As a result, most of them can only handle several simplified cases of the classical degradation model, and are a far cry from real-world SR solutions. Other works [45, 48, 53, 57] resort to the synthesis power of Generative Adversarial Networks (GANs) to generate the missing textures. Although effective, these approaches are prone to artifacts due to the notorious unstable GAN training. Instead of “guessing” the missing textures, another line of research [20, 49, 61, 62] takes advantages of reference images. Their performance is therefore determined by the reference HR images, which are not always available. Addressing this issue, recent works [37, 44] turned to implicit high-resolution priors implemented by *pretrained* GANs. Although bypassing the needs of explicit HR references, these methods are limited to the domain of the pretrained GANs (e.g., face images [3, 50]) and cannot generalize to natural images with diverse contents¹.

In this paper, we propose a novel SR framework based on feature matching, namely FeMaSR, for blind SR of real-world images. The distinct advantage of our framework is that it addresses the aforementioned limitations of previous works by matching LR features to a set of HR features in the pretrained implicit HR priors (HRP). Inspired by the recent VQ-VAE [36, 40] and VQGAN [9], we define our HRP as the combination of a discrete codebook consisting of a pre-defined number of feature vectors and the corresponding pretrained decoder. The feature vectors contain the information of realistic textures that can be decoded into the target HR images. In this way, we break blind SR into two sub-tasks: i) learning a high-quality HRP; ii) mapping the features of LR inputs to the codebook in HRP for distortion removal and detail recovery. For the first sub-task, we

pre-train our HRP with a VQGAN that aims to reconstruct the input HR patches. However, instead of using the vanilla VQGAN, we incorporate semantic information into HRP via L2 regularization with perceptual features from VGG19, thereby enhancing the correlation between semantics and codebook features. For the second sub-task, we follow SwinIR [28] and utilize several swin transformer blocks to encode the LR inputs. The LR encoder is then trained with losses between LR features and ground truth HR features selected from the pretrained codebook. Especially, we found that the feature matching loss is difficult to optimize with fixed HRP. To solve this problem, we introduce multi-scale residual shortcut connections from LR feature space to decoder features. These residual connections enable direct gradient flow from pretrained decoder to the LR encoder, thus making it easier to optimize the LR encoder. Besides, it also helps to complement the possible feature matching errors. Since HRP contains rich semantic-aware HR information of natural images, the proposed FeMaSR is able to recover higher quality textures, see Fig. 1. Our contributions can be summarized as follows:

- We propose a novel framework FeMaSR for blind SR using HRP encoded by a pretrained VQGAN network. Compared with previous works, the FeMaSR formulates SR as a feature matching problem between LR features and distortion-free HR priors, and therefore enables the generation of more realistic images with less artifacts for real-world SR.
- We introduce semantic regularization for the pretrain of semantic-aware HRP. Such a regularization enhances the correlation between semantics and HRP, thereby facilitating the generation of more realistic textures.
- We design a LR encoder with residual shortcut connections to the HRP for feature matching. The proposed framework can better match the LR features with distortion free HR features, and also complement the matching errors.

2 RELATED WORK

Single Image Super-Resolution (SISR) Starting from the pioneer SRCNN [8], deep neural networks have dominated the design of modern SR algorithms. Since then, various network architectures have been proposed to improve the performance of SISR. For example, Kim *et al.* [23] proposed a deep version of SRCNN, named VDSR. Thanks to the residual [16] and residual dense blocks [17] that enable training deeper and wider networks, EDSR [29] and RDN [60] were proposed and boosted the performance of SISR. After that, the attention mechanism is also introduced to SISR, such as channel attention [58], spatial attention [4, 35], non-local attention [59], *etc.* Latest works [6, 28] achieve state-of-the-art performance by employing vision image transformers [30]. These models are trained and evaluated in a non-blind manner, e.g., bicubic downsampling and blurring with known parameters, thereby making it difficult to generalize to SISR with the same degradation type but unseen parameters, let alone those with other degradation types. Addressing this issue, Zhang *et al.* developed a series of methods [52, 54, 55] for conditional image restoration, where users can control the outputs by changing the conditioned degradation parameters.

¹To our knowledge, all state-of-the-art GANs that can synthesize high-quality and high-resolution images are dedicated to a specific domain (e.g., StyleGAN [22]).

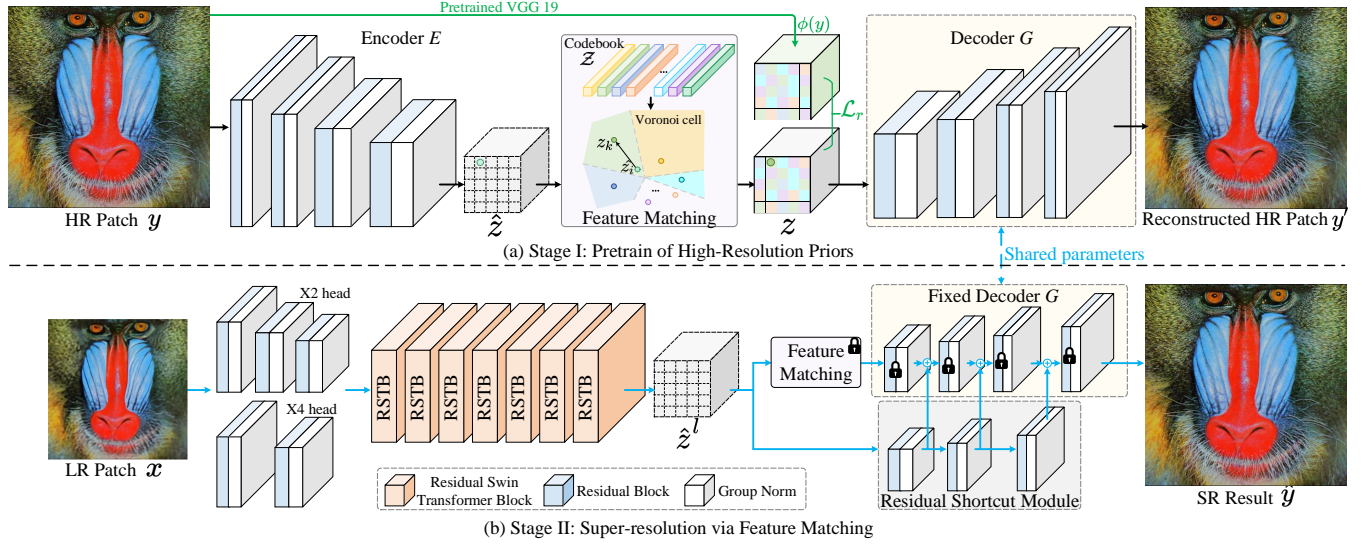


Figure 2: Framework of the proposed FeMaSR. It contains two stages: pretrain of high-resolution prior, and super-resolution via feature matching. We first pretrain a VQGAN to learn an implicit representation of high-resolution patches, i.e., the codebook \mathcal{Z} and decoder G . Then the LR encoder E_l is optimized to find the best matching features of the LR inputs x in the codebook \mathcal{Z} . Since \mathcal{Z} and G are pretrained to reconstruct high resolution patches, FeMaSR is able to generate clearer results with less artifacts.

Blind SISR Upon the performance saturation of non-blind SISR, recent works turned to the more challenging real-world SISR with unknown degradation (*a.k.a.* blind SISR). In general, they model complex real-world degradations in either an implicit or an explicit way. Between them, implicit methods [10, 32, 42, 43, 48] aim to learn a degradation network from real-world LR images. In the absence of corresponding ground truth HR images, most of them employed unsupervised image-to-image translation (*e.g.*, Cycle-GAN [65]) while some recent works [51] resort to contrastive learning. On the contrary, explicit methods aim to synthesize “real” LR images by a manually designed degradation process. Specifically, BSRGAN[53] and Real-ESRGAN[45] describe different ways to improve the common image degradation pipeline. Both of them demonstrate much better visual quality than implicit methods in blind SISR. Nevertheless, both implicit and explicit methods rely on the generative power of GANs to generate textures. However, GANs are known to have difficulties in distinguishing some real-world textures from similar degradation patterns, which usually lead to unrealistic textures or over-smoothed regions in the resulting HR images.

Prior-based SISR Since SISR is intrinsically an ill-posed problem, prior-based SISR methods take advantages of extra image priors either explicitly or implicitly. Methods based on explicit prior (*a.k.a.* RefSR) rely on one or multiple reference HR images which share the same or similar content with the input LR image. To locate the best reference images, various approaches were proposed, including cross-scale correspondences [62], texture transfer [61], transformer network [49], teacher-student [20], internal graph [64], *etc.* Li *et al.* [25–27] narrow the image space to faces and achieve impressive performance. Although effective, explicit priors (*i.e.*, HR reference images) are not always available for a given real-world LR image.

Therefore, prior-based SISR is more promisingly achieved with a prior distribution (*i.e.*, implicit prior) learnt from a large amount of HR images through GANs or VAEs. Menon *et al.* [33] first proposed to upscale LR faces by searching the latent space of a pretrained StyleGAN generator [22]. Gu *et al.* [14] improved it by introducing more latent codes. Pan *et al.* [38] exploited a BigGAN generator [2] as a prior for versatile image restoration. Although these methods can generate realistic images, they all contain a time-consuming optimization process. Addressing this issue, [3, 44, 50] propose to learn a posterior distribution with a pretrained StyleGAN generator. Specifically, they learn an encoder to project LR images to a latent space shared with the pretrained generator that outputs HR images. Although this approach demonstrates exciting performance for face SR, it hardly works for natural images because learning a GAN for natural images remains a challenging task. In this work, we address the above-mentioned challenge following VQGAN [9] that shows outstanding performance in natural image synthesis and can be regarded as high-quality priors for image synthesis.

3 METHODOLOGY

3.1 Framework Overview

Given an input LR image x with unknown degradations, we aim to restore the corresponding high-resolution image with realistic textures. As shown in Fig. 2, we employ a two-stage framework to pretrain the High-Resolution Priors (HRP) and conduct feature matching sequentially:

- **Stage I, Pretraining of High-Resolution Priors.** We use HR patches to pretrain a VQGAN [9] consisting of an encoder E , a discrete codebook \mathcal{Z} , and a decoder G . Inspired by [46], we train the VQGAN with semantic guidance that

enhances the correlation of textures and semantics. We call the codebook \mathcal{Z} and decoder G HRP. After pretraining, our HRP approximately encodes the complete information of HR images and allows the reconstruction of them by feeding their corresponding feature codes $z \in \mathcal{Z}$ to G .

- **Stage II, Super-Resolution via Feature Matching.** Given the HRP (*i.e.*, \mathcal{Z} and G) obtained in Stage I, we argue that blind SR is equivalent to a feature matching problem that aims to match the feature codes of LR inputs \hat{z}^l to those of their HR counterparts $z \in \mathcal{Z}$. By feeding G with the correctly matched HR feature codes z , we can obtain the clean and realistic HR images required in blind SR. To address the optimization challenges posed by the quantization process of VQGAN, we further propose the incorporation of a residual shortcut module to the LR encoder. This not only facilitates training but also complements the feature matching errors, which further boosts the quality of the resulting HR images. Details are described in the following sections.

3.2 Pretraining of High-Resolution Priors

We first make a brief review of VQGAN. As illustrated in Fig. 2, the input HR image $\mathbf{y} \in \mathbb{R}^{H \times W \times 3}$ is first passed through the encoder E to produce its output feature $\hat{z} = E(\mathbf{y}) \in \mathbb{R}^{h \times w \times n_z}$, where n_z is the feature dimension. Then the discrete representation of \hat{z} is calculated by finding the nearest neighbours of each element $\hat{z}_i \in \mathbb{R}^{n_z}$, in the codebook $\mathcal{Z} \in \mathbb{R}^{K \times n_z}$ as follows:

$$z_i = \mathcal{Z}_k, \quad k = \arg \min_j \|\hat{z}_i - \mathcal{Z}_j\|_2, \quad (1)$$

where $z \in \mathbb{R}^{h \times w \times n_z}$, K is the codebook size, $i \in \{1, 2, \dots, h \times w\}$, and $j \in \{1, 2, \dots, K\}$. After that, \mathbf{y} is reconstructed by z with the decoder G :

$$\mathbf{y}' = G(z) \approx \mathbf{y}, \quad (2)$$

Since the feature quantization operation of Eq. (1) is non-differentiable, we follow [9, 36] and simply copy the gradients from G to E for backpropagation. Therefore, the model and codebook can be trained end-to-end with the following objective function:

$$\mathcal{L}_{VQ}(E, G, \mathcal{Z}) = \|\mathbf{y}' - \mathbf{y}\|_1 + \|\text{sg}[\hat{z}] - z\|_2^2 + \beta \|\text{sg}[z] - \hat{z}\|_2^2, \quad (3)$$

where $\text{sg}[\cdot]$ is the stop-gradient operation, and $\beta = 0.25$ according to [9, 36]. With the pretrained VQGAN, any high resolution images \mathbf{y} from the training set can be reconstructed with their corresponding feature vectors in \mathcal{Z} and the decoder G . We therefore call them HRP in this work.

Semantic Guidance As indicated by the vanilla setting in Eq. (3), the codebook \mathcal{Z} is learned purely by gradient descent where similar patterns are clustered independent of their semantics. Meanwhile, Wang *et al.* [46] pointed out that semantic guidance leads to better texture restoration. This motivates us to incorporate semantic information in the pretraining of VQGAN. To be specific, we regularize the training of codebook \mathcal{Z} with perceptual features from a pretrained VGG19 network by adding a regularization term \mathcal{L}_r to \mathcal{L}_{VQ} and have

$$\mathcal{L}'_{VQ} = \mathcal{L}_{VQ} + \mathcal{L}_r = \mathcal{L}_{VQ} + \gamma \|\text{CONV}(z) - \phi(\mathbf{y})\|_2^2 \quad (4)$$

where CONV denotes a simple convolution layer to match the dimension of z and $\phi(\mathbf{y})$, ϕ denotes the pretrained VGG19, and γ is a weighting factor empirically set to 0.1. Note that we follow [9] and also use perceptual loss and adversarial loss in the pretraining.

In summary, our semantic-guided HRP pretraining encourages the texture restoration to be conditioned on semantics, thereby enabling the restoration of more realistic and natural textures.

3.3 Super-Resolution via Feature Matching

With the pretrained HRP, *i.e.*, \mathcal{Z} and G , the SR task is turned into a feature matching problem between LR inputs \mathbf{x} and \mathcal{Z} . Denote the LR encoder as E_l , the problem can be formulated as

$$\arg \min_{\theta} \mathcal{L}(G(\mathbf{q}[E_l(\mathbf{x}, \theta), \mathcal{Z}]), \mathbf{y}), \quad (5)$$

where θ is the learnable parameter of E_l , $\mathbf{q}[\cdot]$ denotes the feature matching process same as Eq. (1), and \mathcal{L} denotes the loss functions (which will be described in the following section). We first make a brief discussion about why we want to transform the SR task to a feature matching process and how can it help:

As we know, image degradation is inherently a one-to-many mapping subject to different types and levels of degradation. From a mathematical point of view, these degradations can be regarded as offsets of high-quality local features in some feature space, where the type and level of degradation correspond to the direction and distance of the offset respectively. Such offsets overlap with each other, thereby making it difficult to find the correct high-quality correspondence of a degraded feature in the feature space. Heuristically, we address this challenge by mapping a degraded feature to its Euclidean nearest neighbour in a given set of pre-defined high-quality features (*i.e.*, the pretrained codebook \mathcal{Z}). Intuitively, the codebook with discrete features partitions the feature space into non-overlapping cells that form a *degradation-based Voronoi diagram*. As demonstrated in Fig. 2, we define the K feature vectors z_k in \mathcal{Z} as the centers of K Voronoi cells. Given an LR feature \hat{z}_i^l , we compute the Euclidean distance between \hat{z}_i^l and all centers z_k to determine which cell \hat{z}_i^l belongs to², *i.e.*, which z_k it maps to. In this way, realistic and rich textures can be generated as the decoder inputs are mapped to expressive HR features z_k instead of the raw LR features \hat{z}_i^l .

Despite the advantages of feature matching, the optimization of Eq. (5) is quite challenging because of the complex LR inputs. For this purpose, we introduce a powerful LR encoder E_l consisting of two parts: feature extraction module and residual shortcut module.

Feature Extraction As shown in Fig. 2, the design of the feature extraction module basically follows SwinIR [28]. It is composed of a shallow feature extraction head and a deep feature extraction block. The deep feature extraction block applies the same stack of residual swin transformer layers as SwinIR, while the shallow feature extraction block is slightly different. Since the HRP is fixed, the final upscaling factor S_{up} of the input LR image is controlled by the downscaling factor S_{down} of the shallow feature encoder block. In this work, we have $S_{up} = S_{down} \times 8$ as the decoder G upscales $z \in$

²In some rare cases (of zero probability), \hat{z}_i^l has the same nearest distances to multiple z_k , *i.e.*, on the boundary of the Voronoi cells. In these cases, we randomly map \hat{z}_i^l to one of the centers.

$\mathbb{R}^{h \times w}$ by $\times 8$. Denote the feature extraction module as H_F , we have:

$$\hat{z}^l = H_F(\mathbf{x}), \quad (6)$$

where $\hat{z}^l \in \mathbb{R}^{h \times w \times n_z}$ are the LR features used for feature matching.

Residual Shortcut Module To better utilize the HRP, we further introduce multi-scale residual connections between \hat{z}^l and the decoder G , as shown in Fig. 2. To be specific, we use several upsampling blocks H_{up} to upscale LR features \hat{z}^l and add them as residuals to the decoder G , *i.e.*,

$$\hat{f}_0 = z, \hat{f}_0 = \hat{z}^l \quad (7)$$

$$\hat{f}_i = G_{up}^i(\hat{f}_{i-1}) + H_{up}^i(\hat{f}_{i-1}), i \in \{1, 2, 3, \dots\} \quad (8)$$

where G_{up}^i and H_{up}^i are the i -th upsampling blocks in G and H_F respectively, \hat{f}_{i-1} and \hat{f}_{i-1} are the input features to them.

Our residual shortcut module has two main benefits. First, it sidesteps the non-differentiable quantization process in VQGAN, thus allowing gradients to be backpropagated directly from G to E_l , which greatly eases the optimization difficulty. Second, we observed that these extra residual connections have also learned to complement the potential errors in feature matching and can further boost the performance of blind SR.

3.4 Training Objectives

The gradients to update E_l come from three parts: feature matching losses, image reconstruction losses, and adversarial loss.

Feature Matching Loss This loss is dedicated to the training of E_l . We first obtain the ground truth latent representation of \mathbf{y} , *i.e.*, $z_{gt} = \mathbf{q}[E(\mathbf{y}), \mathcal{Z}]$, and then calculate the L2 loss and the Gram matrix loss for LR features

$$\mathcal{L}_{fema} = \beta \|\hat{z}^l - z_{gt}\|_2^2 + \alpha \|\psi(\hat{z}^l) - \psi(z_{gt})\|_2^2, \quad (9)$$

where ψ calculates the Gram matrix of features, and α is its weight. The Gram matrix loss, also called style loss, has been shown to be helpful to restore textures [12].

Reconstruction Loss We follow [9, 44] and employ L1 and perceptual losses as our reconstruction loss, formulated as

$$\mathcal{L}_{rec} = \lambda_{L1} \|\hat{\mathbf{y}} - \mathbf{y}\|_1 + \lambda_{per} \|\phi(\hat{\mathbf{y}}) - \phi(\mathbf{y})\|_2^2 \quad (10)$$

where ϕ is a pretrained VGG-16 network, λ_{L1} and λ_{per} are weights of the L1 and perceptual losses respectively.

Adversarial Loss Although our HRP already contains rich texture information, we still need an adversarial loss to help us find better-matching features in the feature matching process. We follow [45] and adopt a U-Net discriminator D with spectral normalization [34]. Similar to [5], we use a hinge loss and define the generator loss as

$$\mathcal{L}_{adv} = \lambda_{adv} \sum_i -\mathbb{E}[D(\hat{\mathbf{y}}_i)] \quad (11)$$

For simplicity, the discriminator loss is omitted here.

Overall Loss The overall loss is defined as

$$\mathcal{L}_{total} = \mathcal{L}_{fema} + \mathcal{L}_{rec} + \mathcal{L}_{adv} \quad (12)$$

where the weights for each loss are set as: $\alpha = \lambda_{L1} = \lambda_{per} = 1, \beta = 0.25, \lambda_{adv} = 0.1$.

4 IMPLEMENTATION DETAILS

4.1 Datasets and Evaluation Metrics

Training Dataset We follow BSRGAN [53] and build a training set that includes DIV2K [1], Flickr2K [29], DIV8K [15] and 10,000 face images from FFHQ [21]. We use the following ways to generate the training patches: (1) crop non-overlapping 512×512 patches; (2) filter patches with few textures; (3) for well-aligned faces in FFHQ, we perform random resize with scale factors between $[0.5, 1.0]$ before cropping to avoid content bias. More details are provided in the supplementary material. The final training dataset contains 136,205 HR patches of size 512×512 . We use the same degradation model as BSRGAN³ to generate corresponding LR images.

Synthetic Testing Dataset To ensure a fair comparison, we use a mixed degradation model of two recent works BSRGAN and RealESRGAN, denoted as `bsrgan_plus`⁵, to generate LR testsets for DIV2K validation set and 5 classical benchmarks, *i.e.*, Set5, Set14, BSD100, Urban100 and Manga109. The diversity of test images guarantees a comprehensive evaluation of model performance.

Real-world Testing Dataset We test our model on three recent real-world benchmarks, including RealSR [44], DRealSR [47] and DPED-iphone [18]. We test models with an upscale factor of 4 for these real-world datasets. Images from RealSR and DRealSR are captured by DSLR cameras, and contain 100 and 93 images respectively. DPED-iphone includes 100 LR images captured by smartphone cameras. The LR images in DPED-iphone are usually more corrupted than those from RealSR and DRealSR.

Evaluation Metrics For synthetic test datasets with ground truth images, we employ the well-known perceptual metric, LPIPS [56] score, to evaluate the perceptual quality of generated images. We also report the results of the widely used PSNR, SSIM scores for references. For real-world benchmarks, there are usually no ground truth images, therefore we adopt the well-known no reference metric NIQE score for quantitative comparison.

4.2 Training Details

In both the HRP pretraining and SR training, we use an Adam [24] optimizer with $\beta_1 = 0.9, \beta_2 = 0.99$. The learning rates for both the generator and discriminator are fixed as 0.0001 throughout the training. During feature matching stage, the codebook \mathcal{Z} and decoder G are fixed. Both our HRP and SR networks are trained with a batch size of 16, and the HR image size is fixed as 256×256 for both $\times 2$ and $\times 4$ upscale factors. We implemented our model with PyTorch [39]. The model pretraining stage takes about 3 days on 2 GeForce RTX 3090 GPUs and the SR stage takes about 4 days on the same device.

5 EXPERIMENTS

5.1 Visualization of HRP

In this experiment, we visualize the features in the codebook \mathcal{Z} with pretrained G , which facilitates the understanding of the proposed framework by answering two questions: i) what priors are encoded in HRP ii) how are they correlated to the semantics?

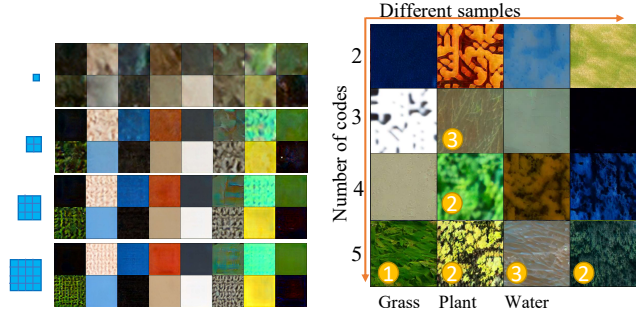
³<https://github.com/cszn/BSRGAN>

Table 1: Quantitative comparison with state-of-the-art methods on synthetic benchmarks. LR images are generated with a mixed degradation model of BSRGAN [53] and Real-ESRGAN [45]. PSNR/SSIM \uparrow : the higher, the better; LPIPS \downarrow : the lower, the better. LPIPS scores can better reflect texture quality, and the best and second performance are marked in red and blue.

Method	Scale	DIV2K Valid			Set5			Set14			BSD100			Urban100			Manga109		
		PSNR	SSIM	LPIPS	PSNR	SSIM	LPIPS	PSNR	SSIM	LPIPS	PSNR	SSIM	LPIPS	PSNR	SSIM	LPIPS	PSNR	SSIM	LPIPS
CDC	$\times 2$	24.93	0.6293	0.6588	25.35	0.6747	0.5153	22.74	0.5347	0.6229	23.64	0.5282	0.7073	20.94	0.5118	0.7001	21.60	0.6345	0.5723
DAN	$\times 2$	24.69	0.5729	0.6219	25.27	0.6278	0.4658	22.79	0.5083	0.5639	23.46	0.4923	0.6384	20.93	0.4793	0.6603	21.78	0.5832	0.5639
DASR(W)	$\times 2$	24.74	0.5767	0.6304	25.31	0.6312	0.4735	22.81	0.5110	0.5720	23.49	0.4958	0.6508	20.94	0.4819	0.6696	21.80	0.5878	0.5587
BSRGAN	$\times 2$	26.60	0.7073	0.3182	27.65	0.7799	0.2027	24.59	0.6475	0.3013	24.88	0.5967	0.3769	22.76	0.6391	0.3199	24.64	0.7678	0.2285
Real-ESRGAN+	$\times 2$	25.50	0.6963	0.2993	26.73	0.7771	0.2157	23.65	0.6299	0.3023	24.11	0.5860	0.3433	21.66	0.6148	0.2876	23.88	0.7698	0.2135
SwinIR-GAN	$\times 2$	25.33	0.6886	0.3313	27.07	0.7793	0.2093	23.76	0.6364	0.3128	23.83	0.5717	0.3707	21.54	0.6195	0.3003	23.56	0.7705	0.2283
Ours	$\times 2$	25.26	0.6680	0.2753	26.46	0.7470	0.1964	23.38	0.5982	0.2852	23.83	0.5599	0.3264	21.90	0.5956	0.2777	23.64	0.7407	0.2192
CDC	$\times 4$	23.11	0.5850	0.7132	19.99	0.5077	0.7168	20.38	0.4551	0.7377	21.75	0.4800	0.7707	19.42	0.4568	0.7345	19.92	0.5834	0.6102
DAN	$\times 4$	24.22	0.5929	0.6881	20.85	0.5319	0.6771	21.44	0.4937	0.6758	22.52	0.4818	0.7438	20.20	0.4757	0.7228	21.02	0.5963	0.6198
DASR(W)	$\times 4$	24.19	0.5920	0.7021	20.87	0.5336	0.6972	21.43	0.4953	0.6950	22.49	0.4818	0.7576	20.18	0.4752	0.7400	21.03	0.5975	0.6319
BSRGAN	$\times 4$	24.91	0.6500	0.3596	21.63	0.5573	0.4683	22.17	0.5165	0.4173	22.95	0.5042	0.4405	20.91	0.5386	0.3874	22.45	0.6968	0.3039
Real-ESRGAN+	$\times 4$	23.80	0.6414	0.3696	21.31	0.5449	0.5068	21.54	0.5288	0.4271	22.43	0.5035	0.4693	19.90	0.5282	0.3838	21.97	0.6989	0.3073
SwinIR-GAN	$\times 4$	24.13	0.6479	0.3543	20.91	0.5128	0.5115	21.58	0.5041	0.4487	22.23	0.4925	0.4447	20.01	0.5300	0.3592	22.21	0.7007	0.3044
Ours	$\times 4$	23.77	0.6203	0.3298	20.45	0.4863	0.4942	21.24	0.4809	0.3801	22.11	0.4830	0.4143	20.25	0.5243	0.3566	21.98	0.6816	0.2846

Table 2: Quantitative comparison with state-of-the-art methods on real-world benchmarks. NIQE \downarrow : the lower, the better. The best and second performance are marked in red and blue. Some numbers of competitive methods are taken from [45].

Datasets	Bicubic	DAN	RealSR	CDC	DASR(W)	BSRGAN	Real-ESRGAN+	SwinIR-GAN	Ours
RealSR [44]	6.2438	6.5673	6.8041	6.2376	8.1918	5.7355	4.7832	4.7644	4.7434
DRealSR [47]	6.5766	7.0720	7.7213	6.6359	9.1446	6.1362	4.8458	4.7053	4.1987
DPED-iphone [18]	6.0121	6.1414	5.5855	6.2738	6.9887	5.9906	5.2631	4.9468	5.1066



(a) Textures generated with tiled single code. The tiled feature size are: 1×1 , 2×2 , 3×3 , 4×4 (from top to bottom)
 (b) Textures generated with random combination with different number of codes. The size of combined feature map is 16×16 .

Figure 3: Visualization of texture priors encoded with pre-trained codebook \mathcal{Z} . Semantic textures emerge when different codes are combined, such as ① grass, ② plant and ③ water.

As shown in Fig. 3, we visualize the priors encoded in \mathcal{Z} by projecting features to RGB pixel space with pretrained decoder G . In other words, we obtain the RGB patches of each vector $z_j \in \mathcal{Z}$

with $G(z_j)$, where the size of RGB patches is 8×8 . Specifically, we explore how textures are encoded by single codes and combinations of different codes:

- Fig. 3(a) shows that individual codes alone can represent some basic texture elements. However, when the same code is tiled onto a bigger feature map, e.g., 4×4 , the decoder tends to preserve the color while producing a smooth image. This implies that a single code is not enough to represent complex textures.
- Fig. 3(b) shows that complex and realistic textures can be generated by combining several different code samples, which indicates that the pretrained \mathcal{Z} indeed learns to encode rich texture priors. In addition, it can be observed that different combinations of code samples correspond to different semantics, such as ① grass, ② plant and ③ water. Please see the supplementary materials for more examples.

Based on the above discussion, we conjecture that the individual codes in \mathcal{Z} represent simple texture elements, while the diverse semantics are encoded in the combinations of multiple codes.

5.2 Comparison with Existing Methods

We compare the proposed QuanTexSR with several state-of-the-art methods for blind SR, including CDC [47], DAN [31], DASR(W) [43], RealSR [19], BSRGAN [53], Real-ESRGAN+ [45] and SwinIR-GAN

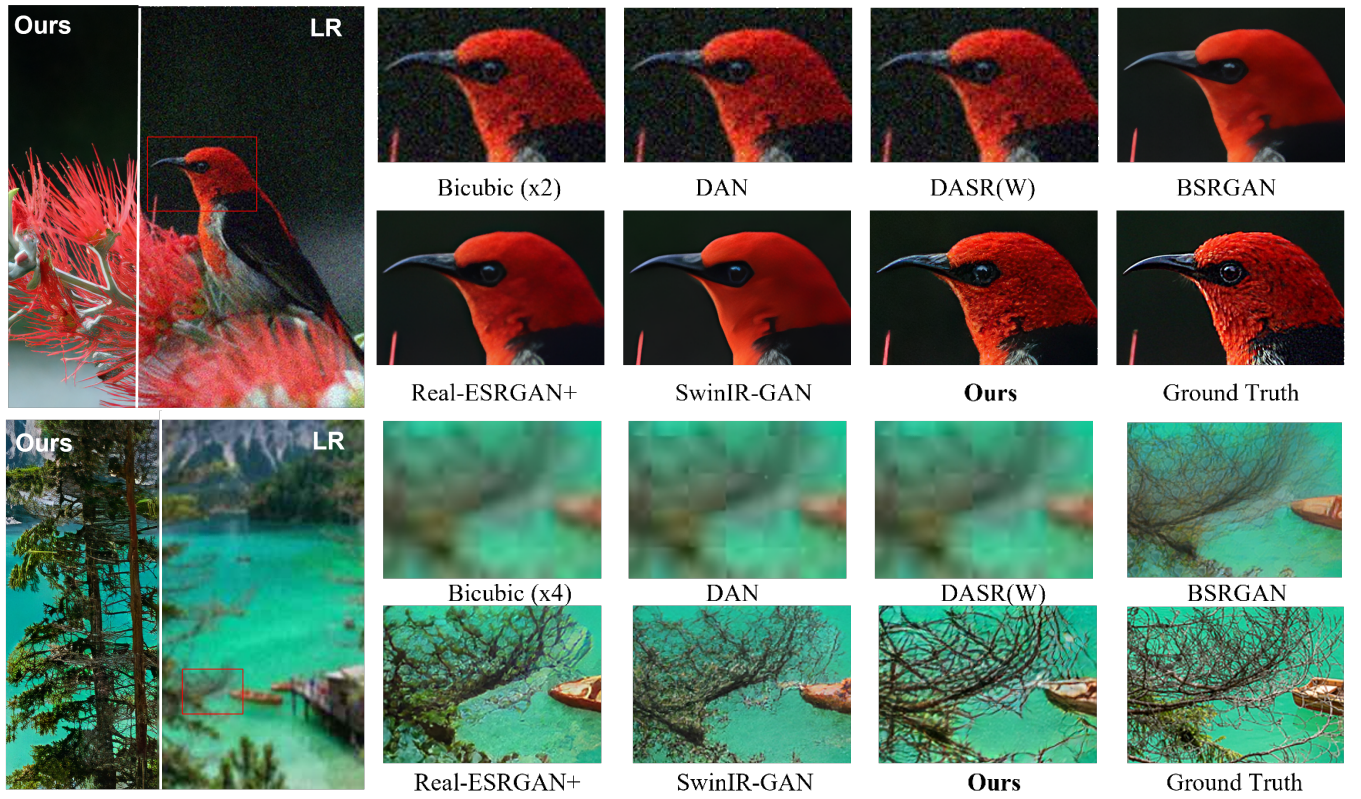


Figure 4: Visual comparisons on two examples from synthesize benchmarks with upscale factor of 2 (first row) and 4 (second row). Thanks to the HRP, our model is able to restore realistic and faithful textures even when the inputs are severely corrupted. As for the competitive works, some have difficulties to remove degradation, *i.e.*, DAN and DASR(W), and the others generate artifacts or tend to be oversmooth, *i.e.*, BSRGAN, Real-ESRGAN+, SwinIRGAN. **Please zoom in for best view.**

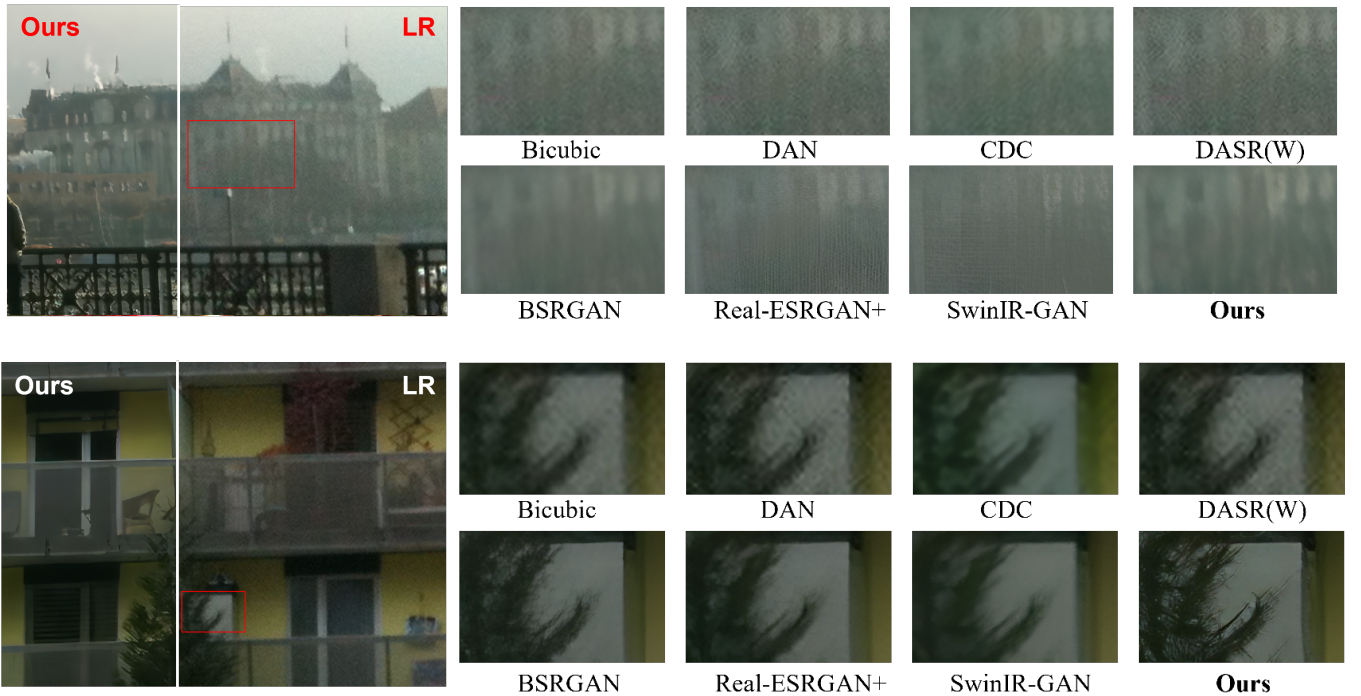


Figure 5: Visual comparisons on two real-world example with upscale factor 4. Our model can remove degradations and generate feasible details at the same time, while other GAN based methods tend to be either over-textured (first row) or over-smooth (second row). **Please zoom in for best view.**

[28]. Specifically, CDC proposed a divide-and-conquer architecture; DAN, DASR(W) and RealSR learned degradation models from LR inputs; BSRGAN, Real-ESRGAN+ and SwinIR-GAN used synthetic training data generated by handcrafted degradation models. We use the original codes and weights from the official public github repositories for all competing methods. Quantitative and qualitative results on both synthetic and real-world benchmarks are reported as follows.

Comparison on Synthetic Benchmarks As Tab. 1 shows, our QuanTexSR outperforms competing methods in LPIPS scores on most benchmarks (5 out of 6). Note that we focus on the LPIPS scores as it better captures the perceptual quality than other metrics (e.g., PSNR/SSIM) [44, 45, 50, 53, 56]. In addition, it can be observed that: in general, methods that learn the degradations, such as DAN and DASR(W), perform much worse than those using manually designed degradation models, which indicates the difficulties in learning complex real-world degradations. Furthermore, we compare the SR results qualitatively through visual inspection in Fig. 4. It can be observed that in the first row, BSRGAN, Real-ESRGAN and SwinIR-GAN mistake the feather textures as noises and remove them. And in the second row, although the distortions are removed successfully, they all fail to generate feasible textures for the trees. In contrast, thanks to the semantic-aware HRP, our method does not have such problems and generates higher quality results.

Comparison on Real-world Benchmarks To make a fair comparison, we compare our method against state-of-the-art ones on three large real-world benchmarks and evaluate the results using a standard no-reference IQA metric NIQE. As Tab. 2 shows, our method outperforms competing methods in 2 out of 3 real-world benchmarks, which clearly demonstrates the effectiveness of our framework. In Fig. 5, it can be observed that our FeMaSR produces sharp and clear textures without generating artifacts, while the other methods either fail to remove degradations or tend to be over-textured and over-smooth. Please see the supplementary materials for more results.

5.3 Ablation Study

We conduct ablation experiments on four variations of our framework as shown in Tab. 3 to validate our design: Model-A, a baseline network by discarding Stage I, feature matching and residual shortcuts. It has a similar architecture with SwinIR, and is trained with GAN from scratch; Model-B, Model-A with pretrained decoder; Model-C, Model-B with pretrained codebook and feature matching; FeMaSR, full model with HRP and residual shortcuts; Model-D, FeMaSR based on HRP without semantic guidance.

Effectiveness of Residual Shortcut As claimed in Sec. 3, residual shortcut helps optimization of feature matching process and complements possible matching errors. We verify them by removing the residual shortcut in training (Model-C) and testing stage respectively. As we can see in Fig. 6(a), the feature matching loss \mathcal{L}_{fema} decreases much faster with residual shortcut. This indicates that residual shortcut is essential for the optimization of \mathcal{L}_{fema} . We can also observe a clear performance drop of model C without residual shortcut in Tab. 3 and Fig. 7. We further demonstrate how residual shortcut helps to complement feature matching errors in Fig. 6(b). We can notice that model with disabled residual shortcut

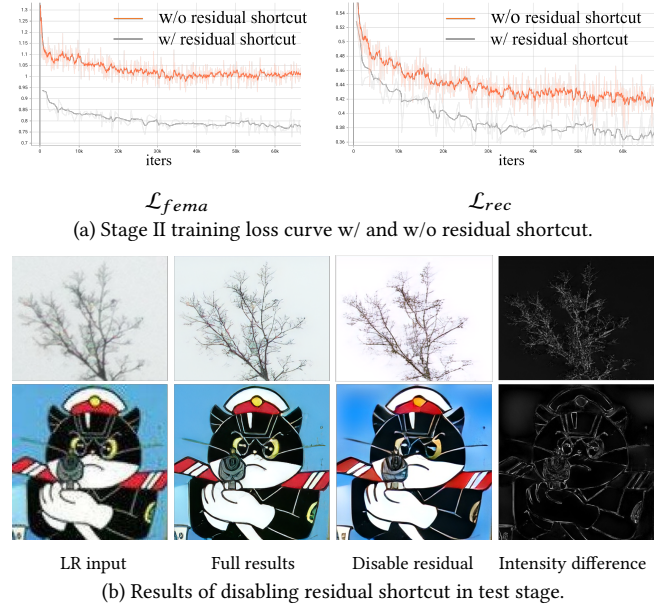


Figure 6: Effectiveness of residual shortcut.

Table 3: Ablation study on synthetic benchmark DIV2K Valid with upscale factor of 2.

Model ID	Model Variations	LPIPS↓
A	w/o HRP	0.3025
B	+ pretrained decoder	0.2944
C	+ pretrained codebook (with feature matching)	0.3358
FeMaSR	+ residual	0.2753
D	FeMaSR w/o semantic	0.2887

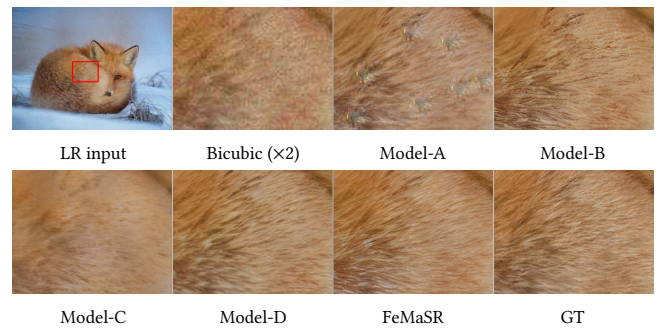


Figure 7: Visual examples of different model variations. Please zoom in for best view.

can already remove the distortions to a large extent. The residual shortcut mainly complements the color and edges.

Effectiveness of HRP Model-[A, B and FeMaSR] validate the necessities of \mathcal{Z} and G in HRP. As discussed above, the performance drop of Model-C is mainly due to the optimization difficulty brought

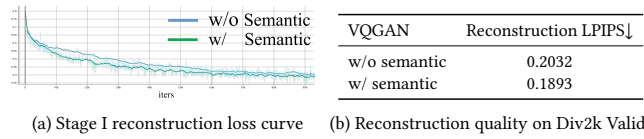


Figure 8: Effectiveness of semantic guidance.

by feature matching. Therefore, we do not use it to validate HRP. It can be observed that Model-B is better than Model-A since the pretrained decoder helps to stabilize GAN training. However, both Model-A and Model-B cannot handle complex distortions without feature matching and tend to generate artifacts, see Fig. 7. Meanwhile, the full model, FeMaSR, can make full use of HRP in both G and Z , and thereby has the best performance.

Effectiveness of Semantic Guidance We provide reconstruction training loss curve and LPIPS score in Stage I to show the benefits of semantic guidance. It can be seen that VQGAN with semantic guidance converges faster and performs better, resulting in a better HRP. This finally helps to improve the restoration performance, see Tab. 3 and Fig. 7.

6 CONCLUSION

In this paper, we have investigated the usage of implicit high-resolution priors (HRP) encoded in the codebook and associated decoder of a pretrained VQGAN for real-world blind SR. In particular, we formulate the SR task to a feature matching problem between the LR features and distortion free HR feature codebook. Because HRP is distortion free and fixed during SR stage, our FeMaSR is able to generate more realistic results with less artifacts than previous GAN based approaches. To train a better HRP, we integrate semantic information to HRP with features from pretrained VGG19 network. To facilitate optimization of feature matching loss, we introduce multi-scale residual shortcut connections to the pretrained decoder. Quantitative and qualitative experiments on both synthetic and real-world benchmarks demonstrate the superiority of the proposed FeMaSR for real-world LR images.

7 ACKNOWLEDGEMENT

This work was done at GAP Lab, CUHKSZ which is directed by Prof. Xiaoguang Han, and is supported by Alibaba Innovative Research, National Natural Science Foundation of China (62072383, 61702433, 62077039), the Fundamental Research Funds for the Central Universities (20720210044, 20720190006).

REFERENCES

- [1] Eirikur Agustsson and Radu Timofte. 2017. NTIRE 2017 Challenge on Single Image Super-Resolution: Dataset and Study. In *CVPRW*.
- [2] Andrew Brock, Jeff Donahue, and Karen Simonyan. 2019. Large Scale GAN Training for High Fidelity Natural Image Synthesis. In *ICLR*.
- [3] Kelvin CK Chan, Xintao Wang, Xiangyu Xu, Jinwei Gu, and Chen Change Loy. 2021. Glean: Generative latent bank for large-factor image super-resolution. In *CVPR*. 14245–14254.
- [4] Chaofeng Chen, Dihong Gong, Hao Wang, Zhifeng Li, and Kwan-Yee K. Wong. 2020. Learning Spatial Attention for Face Super-Resolution. In *IEEE TIP*.
- [5] Chaofeng Chen, Xiaoming Li, Yang Lingbo, Xianhui Lin, Lei Zhang, and KKY Wong. 2021. Progressive Semantic-Aware Style Transformation for Blind Face Restoration. In *CVPR*.
- [6] Hanting Chen, Yunhe Wang, Tianyu Guo, Chang Xu, Yiping Deng, Zhenhua Liu, Siwei Ma, Chunjing Xu, Chao Xu, and Wen Gao. 2021. Pre-Trained Image Processing Transformer. In *CVPR*.
- [7] Tao Dai, Jianrui Cai, Yongbing Zhang, Shu-Tao Xia, and Lei Zhang. 2019. Second-order Attention Network for Single Image Super-Resolution. In *CVPR*. 11065–11074.
- [8] Chao Dong, Chen Change Loy, Kaiming He, and Xiaoou Tang. 2014. Learning a deep convolutional network for image super-resolution. In *ECCV*. Springer, 184–199.
- [9] Patrick Esser, Robin Rombach, and Bjorn Ommer. 2021. Taming transformers for high-resolution image synthesis. In *CVPR*. 12873–12883.
- [10] Manuel Fritsche, Shuhang Gu, and Radu Timofte. 2019. Frequency separation for real-world super-resolution. In *ICCVW*. 3599–3608.
- [11] Leon Gatys, Alexander S Ecker, and Matthias Bethge. 2015. Texture synthesis using convolutional neural networks. *NeurIPS* 28 (2015), 262–270.
- [12] Muhammad Waleed Gondal, Bernhard Schölkopf, and Michael Hirsch. 2018. The unreasonable effectiveness of texture transfer for single image super-resolution. In *ECCVW*. Springer, 80–97.
- [13] Jinjin Gu, Hannan Lu, Wangmeng Zuo, and Chao Dong. 2019. Blind super-resolution with iterative kernel correction. In *CVPR*. 1604–1613.
- [14] Jinjin Gu, Yujun Shen, and Bolei Zhou. 2020. Image processing using multi-code gan prior. In *CVPR*. 3012–3021.
- [15] Shuhang Gu, Andreas Lugmayr, Martin Danelljan, Manuel Fritsche, Julien Lamour, and Radu Timofte. 2019. Div8k: Diverse 8k resolution image dataset. In *ICCVW*. IEEE, 3512–3516.
- [16] Kaiming He, Xiangyu Zhang, Shaoqing Ren, and Jian Sun. 2016. Deep residual learning for image recognition. In *CVPR*. 770–778.
- [17] Gao Huang, Zhuang Liu, Laurens Van Der Maaten, and Kilian Q Weinberger. 2017. Densely connected convolutional networks. In *CVPR*. 4700–4708.
- [18] Andrey Ignatov, Nikolay Kobyshev, Radu Timofte, Kenneth Vanhoey, and Luc Van Gool. 2017. Dslr-quality photos on mobile devices with deep convolutional networks. In *ICCV*. 3277–3285.
- [19] Xiaozhong Ji, Yun Cao, Ying Tai, Chengjie Wang, Jilin Li, and Feiyue Huang. 2020. Real-world super-resolution via kernel estimation and noise injection. In *CVPRW*. 466–467.
- [20] Yuning Jiang, Kelvin CK Chan, Xintao Wang, Chen Change Loy, and Ziwei Liu. 2021. Robust Reference-based Super-Resolution via C2-Matching. In *CVPR*. 2103–2112.
- [21] Tero Karras, Timo Aila, Samuli Laine, and Jaakko Lehtinen. 2018. Progressive growing of gans for improved quality, stability, and variation. *ICLR* (2018).
- [22] Tero Karras, Samuli Laine, Miika Aittala, Janne Hellsten, Jaakko Lehtinen, and Timo Aila. 2020. Analyzing and improving the image quality of stylegan. In *CVPR*. 8110–8119.
- [23] Jiwon Kim, Jung Kwon Lee, and Kyoung Mu Lee. 2016. Accurate image super-resolution using very deep convolutional networks. In *CVPR*. 1646–1654.
- [24] Diederik P Kingma and Jimmy Ba. 2014. Adam: A method for stochastic optimization. *arXiv preprint arXiv:1412.6980* (2014).
- [25] Xiaoming Li, Chaofeng Chen, Shangchen Zhou, Xianhui Lin, Wangmeng Zuo, and Lei Zhang. 2020. Blind face restoration via deep multi-scale component dictionaries. In *ECCV*. Springer, 399–415.
- [26] Xiaoming Li, Wenyu Li, Dongwei Ren, Hongzhi Zhang, Meng Wang, and Wangmeng Zuo. 2020. Enhanced blind face restoration with multi-exemplar images and adaptive spatial feature fusion. In *CVPR*. 2706–2715.
- [27] Xiaoming Li, Ming Liu, Yuting Ye, Wangmeng Zuo, Liang Lin, and Ruigang Yang. 2018. Learning warped guidance for blind face restoration. In *ECCV*. 272–289.
- [28] Jingyun Liang, Jiezhang Cao, Guolei Sun, Kai Zhang, Luc Van Gool, and Radu Timofte. 2021. SwinIR: Image Restoration Using Swin Transformer. In *ICCVW*.
- [29] Bee Lim, Sanghyun Son, Heewon Kim, Seungjun Nah, and Kyoung Mu Lee. 2017. Enhanced deep residual networks for single image super-resolution. In *CVPRW*. 136–144.
- [30] Ze Liu, Yutong Lin, Yue Cao, Han Hu, Yixuan Wei, Zheng Zhang, Stephen Lin, and Baining Guo. 2021. Swin transformer: Hierarchical vision transformer using shifted windows. *ICCV* (2021).
- [31] Zhengxiong Luo, Yan Huang, Shang Li, Liang Wang, and Tieniu Tan. 2020. Unfolding the Alternating Optimization for Blind Super Resolution. *NeurIPS* 33 (2020).
- [32] Shunta Maeda. 2020. Unpaired image super-resolution using pseudo-supervision. In *CVPR*. 291–300.
- [33] Sachit Menon, Alexandru Damian, Shijia Hu, Nikhil Ravi, and Cynthia Rudin. 2020. Pulse: Self-supervised photo upsampling via latent space exploration of generative models. In *CVPR*. 2437–2445.
- [34] Takeru Miyato, Toshiki Kataoka, Masanori Koyama, and Yuichi Yoshida. 2018. Spectral Normalization for Generative Adversarial Networks. In *ICLR*.
- [35] Ben Niu, Weiwei Wen, Wenqi Ren, Xiangde Zhang, Lianping Yang, Shuzhen Wang, Kaihao Zhang, Xiaochun Cao, and Haifeng Shen. 2020. Single image super-resolution via a holistic attention network. In *ECCV*. Springer, 191–207.
- [36] Aaron van den Oord, Oriol Vinyals, and Koray Kavukcuoglu. 2017. Neural discrete representation learning. *NeurIPS* (2017).
- [37] Xingang Pan, Xiaohang Zhan, Bo Dai, Dahua Lin, Chen Change Loy, and Ping Luo. 2020. Exploiting Deep Generative Prior for Versatile Image Restoration and Manipulation. In *ECCV*.

- [38] Xingang Pan, Xiaohang Zhan, Bo Dai, Dahua Lin, Chen Change Loy, and Ping Luo. 2020. Exploiting deep generative prior for versatile image restoration and manipulation. In *ECCV*. Springer, 262–277.
- [39] Adam Paszke, Sam Gross, Francisco Massa, Adam Lerer, James Bradbury, Gregory Chanan, Trevor Killeen, Zeming Lin, Natalia Gimelshein, Luca Antiga, Alban Desmaison, Andreas Kopf, Edward Yang, Zachary DeVito, Martin Raison, Alykhan Tejani, Sasank Chilamkurthy, Benoit Steiner, Lu Fang, Junjie Bai, and Soumith Chintala. 2019. PyTorch: An Imperative Style, High-Performance Deep Learning Library. In *NeurIPS*, Vol. 32. 8026–8037.
- [40] Ali Razavi, Aaron van den Oord, and Oriol Vinyals. 2019. Generating diverse high-fidelity images with vq-vae-2. In *NeurIPS*. 14866–14876.
- [41] Assaf Shocher, Nadav Cohen, and Michal Irani. 2018. “zero-shot” super-resolution using deep internal learning. In *CVPR*. 3118–3126.
- [42] Ziyu Wan, Bo Zhang, Dongdong Chen, Pan Zhang, Dong Chen, Jing Liao, and Fang Wen. 2020. Bringing old photos back to life. In *CVPR*. 2747–2757.
- [43] Longguang Wang, Yingqian Wang, Xiaoyu Dong, Qingyu Xu, Jungang Yang, Wei An, and Yulan Guo. 2021. Unsupervised Degradation Representation Learning for Blind Super-Resolution. In *CVPR*. 10581–10590.
- [44] Xintao Wang, Yu Li, Honglun Zhang, and Ying Shan. 2021. Towards Real-World Blind Face Restoration with Generative Facial Prior. In *CVPR*. 9168–9178.
- [45] Xintao Wang, Liangbin Xie, Chao Dong, and Ying Shan. 2021. Real-ESRGAN: Training Real-World Blind Super-Resolution with Pure Synthetic Data. *ICCVW* (2021).
- [46] Xintao Wang, Ke Yu, Chao Dong, and Chen Change Loy. 2018. Recovering realistic texture in image super-resolution by deep spatial feature transform. In *CVPR*.
- [47] Pengxu Wei, Ziwei Xie, Hannan Lu, Zongyuan Zhan, Qixiang Ye, Wangmeng Zuo, and Liang Lin. 2020. Component divide-and-conquer for real-world image super-resolution. In *ECCV*. Springer, 101–117.
- [48] Yunxuan Wei, Shuhang Gu, Yawei Li, Radu Timofte, Longcun Jin, and Hengjie Song. 2021. Unsupervised real-world image super resolution via domain-distance aware training. In *CVPR*. 13385–13394.
- [49] Fuzhi Yang, Huan Yang, Jianlong Fu, Hongtao Lu, and Baining Guo. 2020. Learning Texture Transformer Network for Image Super-Resolution. In *CVPR*.
- [50] Tao Yang, Peiran Ren, Xuansong Xie, and Lei Zhang. 2021. GAN Prior Embedded Network for Blind Face Restoration in the Wild. In *CVPR*. 672–681.
- [51] Jiahui Zhang, Shijian Lu, Fangneng Zhan, and Yingchen Yu. 2021. Blind Image Super-Resolution via Contrastive Representation Learning. *arXiv preprint arXiv:2107.00708* (2021).
- [52] Kai Zhang, Luc Van Gool, and Radu Timofte. 2020. Deep unfolding network for image super-resolution. In *CVPR*. 3217–3226.
- [53] Kai Zhang, Jingyun Liang, Luc Van Gool, and Radu Timofte. 2021. Designing a practical degradation model for deep blind image super-resolution. *ICCV* (2021).
- [54] Kai Zhang, Wangmeng Zuo, and Lei Zhang. 2018. Learning a single convolutional super-resolution network for multiple degradations. In *CVPR*. 3262–3271.
- [55] Kai Zhang, Wangmeng Zuo, and Lei Zhang. 2019. Deep plug-and-play super-resolution for arbitrary blur kernels. In *CVPR*. 1671–1681.
- [56] Richard Zhang, Phillip Isola, Alexei A Efros, Eli Shechtman, and Oliver Wang. 2018. The Unreasonable Effectiveness of Deep Features as a Perceptual Metric. In *CVPR*.
- [57] Wenlong Zhang, Yihao Liu, Chao Dong, and Yu Qiao. 2019. Ranksrgan: Generative adversarial networks with ranker for image super-resolution. In *ICCV*. 3096–3105.
- [58] Yulun Zhang, Kunpeng Li, Kai Li, Lichen Wang, Bineng Zhong, and Yun Fu. 2018. Image super-resolution using very deep residual channel attention networks. In *ECCV*. 286–301.
- [59] Yulun Zhang, Kunpeng Li, Kai Li, Bineng Zhong, and Yun Fu. 2019. Residual Non-local Attention Networks for Image Restoration. In *ICLR*.
- [60] Yulun Zhang, Yapeng Tian, Yu Kong, Bineng Zhong, and Yun Fu. 2018. Residual dense network for image super-resolution. In *CVPR*. 2472–2481.
- [61] Zhifei Zhang, Zhaowen Wang, Zhe Lin, and Hairong Qi. 2019. Image super-resolution by neural texture transfer. In *CVPR*. 7982–7991.
- [62] Haitian Zheng, Mengqi Ji, Haoqian Wang, Yebin Liu, and Lu Fang. 2018. CrossNet: An End-to-end Reference-based Super Resolution Network using Cross-scale Warping. In *ECCV*. 88–104.
- [63] Ruofan Zhou and Sabine Susstrunk. 2019. Kernel modeling super-resolution on real low-resolution images. In *CVPR*. 2433–2443.
- [64] Shangchen Zhou, Jiawei Zhang, Wangmeng Zuo, and Chen Change Loy. 2020. Cross-Scale Internal Graph Neural Network for Image Super-Resolution. In *NeurIPS*.
- [65] Jun-Yan Zhu, Taesung Park, Phillip Isola, and Alexei A Efros. 2017. Unpaired image-to-image translation using cycle-consistent adversarial networks. In *ICCV*. 2223–2232.

A MORE IMPLEMENTATION DETAILS

A.1 Network Architectures of VQGAN

In complementary to the simple network architecture in the paper, we provide details of hyper parameters for the VQGAN encoder and decoder in Fig. 9. We use the codebook f^{LP} with size 1024×512 in our experiment. The input image is of size 256×256 and downsampled into 32×32 feature maps. Convolution layers with “k3n#s1” are used to match feature channels with the codebook feature dimensions before and after the feature quantization process.

We perform experiments to select suitable codebook numbers for our model, see Tab. 4 for the results. It can be observed that more codes generally leads to better reconstruction performance, but the improvements is marginal when the number is sufficiently large. We empirically select 1024 as a good balance between performance and computation cost.

Table 4: VQGAN reconstruction performance with different code numbers.

Codebook number	256	512	1024	2048
Reconstruction LPIPS↓	0.2165	0.2044	0.1893	0.1837

A.2 Details of Synthetic Dataset

Generation of training HR patches. As described in the paper, we use high resolution images from DIV2K [1], Flickr2K [29], DIV8K [15] and 10,000 face images from FFHQ [21] to generate HR training patches of size 512×512 . The overall summary of training images are shown in Tab. 5, and some examples are shown in Fig. 10. Details to obtain the patches are as follow:

For the first three datasets which contains natural images, we crop the patches with the following steps:

- (1) Crop non-overlapping 512×512 patches;
- (2) Filter patches with few textures (or edges). For this purpose, we first calculate the sobel edge map of the patch, then compute mean and variation of the edge map, denoted as μ, σ^2 . Because edge map is sparse, more edges means bigger σ^2 and μ , we therefore empirically filter patches whose $\sigma^2 < 10$;

For the FFHQ face dataset, the images are well-aligned faces of size 1024×1024 . Previous non-overlap cropping would cause content bias for this dataset. Therefore, we first randomly resize the image with scale factor between $[0.5, 1.0]$, and then random crop only one patch from each image.

Online generation of training pairs. We use the same degradation model as BSRGAN [53] to generate corresponding LR images online. To be specific, the input HR patches are first randomly cropped to 256×256 patches, and then degraded with `degradation_bsrgan`⁴ function with scale factors 2 and 4 to generate training pairs.

Generation of synthetic testing benchmarks. For a fair comparison, we use a mixed degradation model of BSRGAN and Real-ESRGAN to synthesize testing LR images. Specifically, we use

`degradation_bsrgan_plus`⁵ function with scale factor 2 and 4 to generate testing pairs with a fixed random seed 123.

B MORE RESULTS

B.1 Visualization of HRP

In this part, we show more empirical visualizations of the learned high-resolution priors (HRP). Firstly, we show an overview of all the 1024 codes separately in Fig. 12. Then, we show visualization of semantic-related codes with the help of a semantic texture datasets, *i.e.*, the OST dataset [46] with the following steps:

- Obtain the codes of each image with pretrained VQGAN. Figure 13 show some examples of the reconstruction results with our model.
- Calculate the distribution of each texture category on the codebook \mathcal{Z} , as shown in Fig. 14
- Sample codes from the distribution of each class and randomly arrange them to compose a 8×8 latent feature z , and then decode it to 64×64 RGB texture patch.

Finally, Figure 15 empirically visualizes the learned HRP on OST dataset. We can observe that codes sampled from different texture distribution generates textures similar to the corresponding semantics, which proves the effectiveness of the HRP. Please note that the texture shapes are closely related with orders of latent codes, Fig. 15 are just empirical statistic visualizations with random arrangement of codes.

B.2 Failure Cases

By observing the results, we empirically discovered a limitation of our proposed FeMaSR: it favors natural textures over artificial textures, *e.g.* the straight lines that dominate the building images. Our method usually generates curved lines instead (see Fig. 11). A similar phenomenon also occurs in neural texture synthesis [11]. We leave the solution of this problem to future work.

B.3 Qualitative Results

We show more results on synthetic datasets in Fig. 16 and real-world test images in Fig. 17

⁴https://github.com/cszn/BSRGAN/blob/main/utils/utils_blindsr.py

⁵https://github.com/cszn/BSRGAN/blob/main/utils/utils_blindsr.py

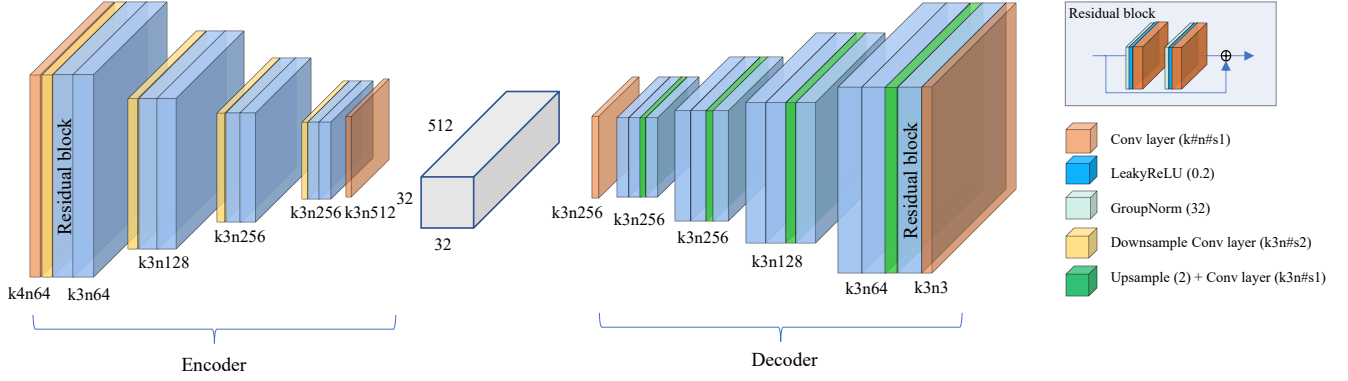


Figure 9: Details of hyper parameters for VQGAN. “k3n64s1” denotes single convolution layer with kernel size 3 × 3, output channel 64 and stride size 1, “#” means the corresponding value. We use group normalization with 32 group numbers, leakyrelu with 0.2 as negative slope. The upsample convolution is a nearest upsample layer with scale factor 2 followed by a convolution layer.

Table 5: Details of HR training datasets.

Dataset	DIV2K	DIV8K	Flickr2K	FFHQ	Total
Number of full image	800	1500	2550	10,000	14,850
Typical image size $W \times H$	2032×1344	6720×3840	2032×1344	1024×1024	-
Number of cropped patches	8257	90,892	27,056	10,000	136,205



Figure 10: Examples of cropped training HR patches.



Figure 11: Failure case: a building image with straight lines.

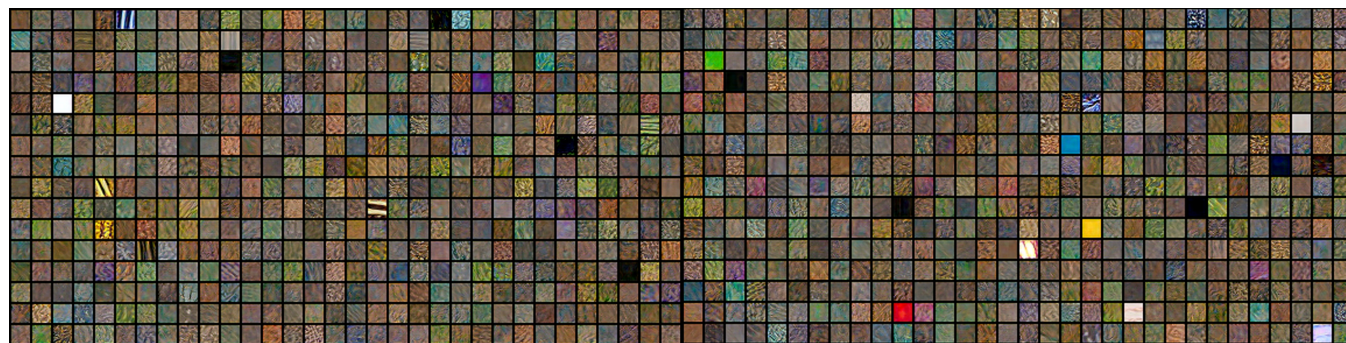


Figure 12: Visualization overview of all the 1024 codes in HRP.

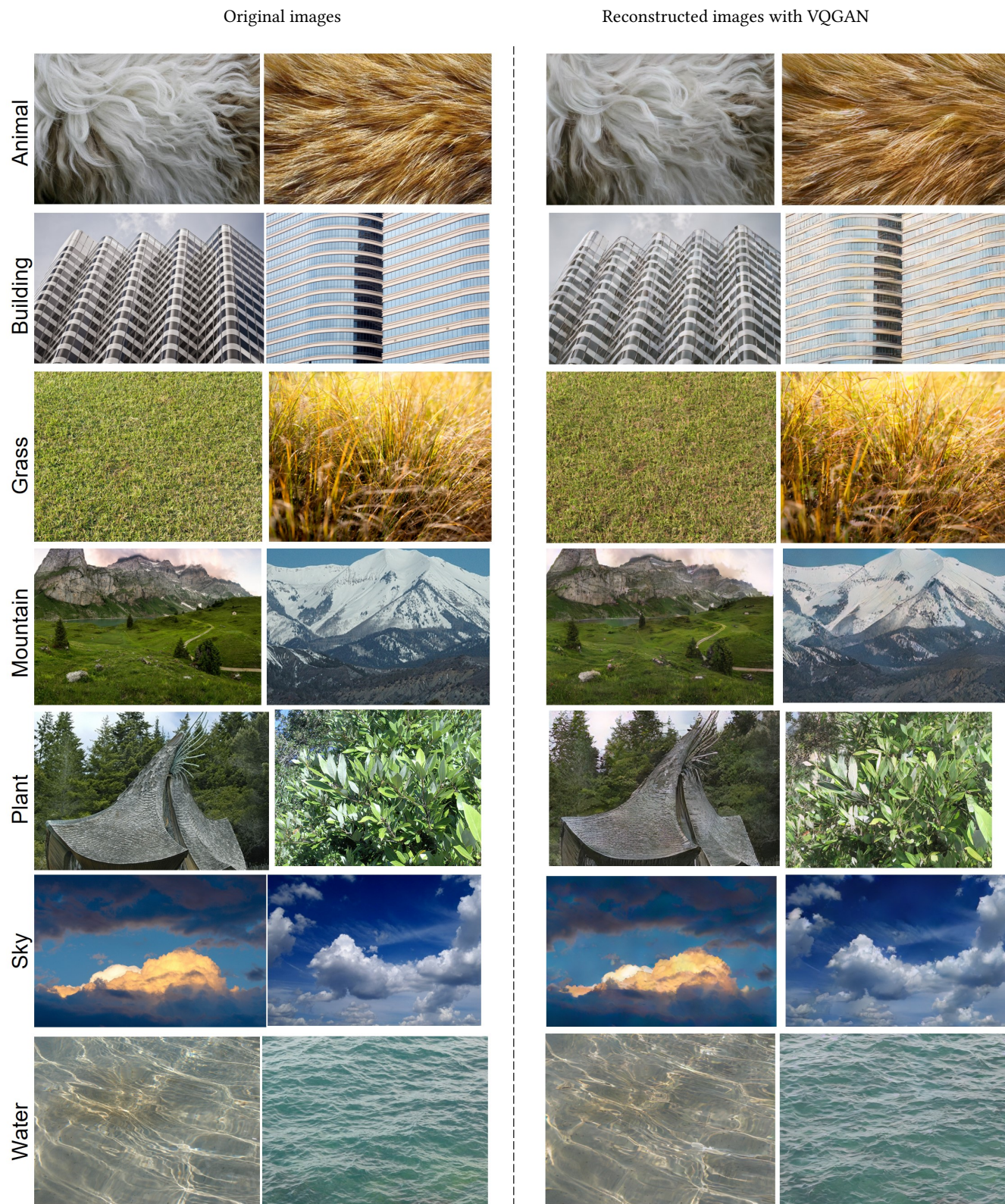


Figure 13: Reconstruction examples from OST dataset.

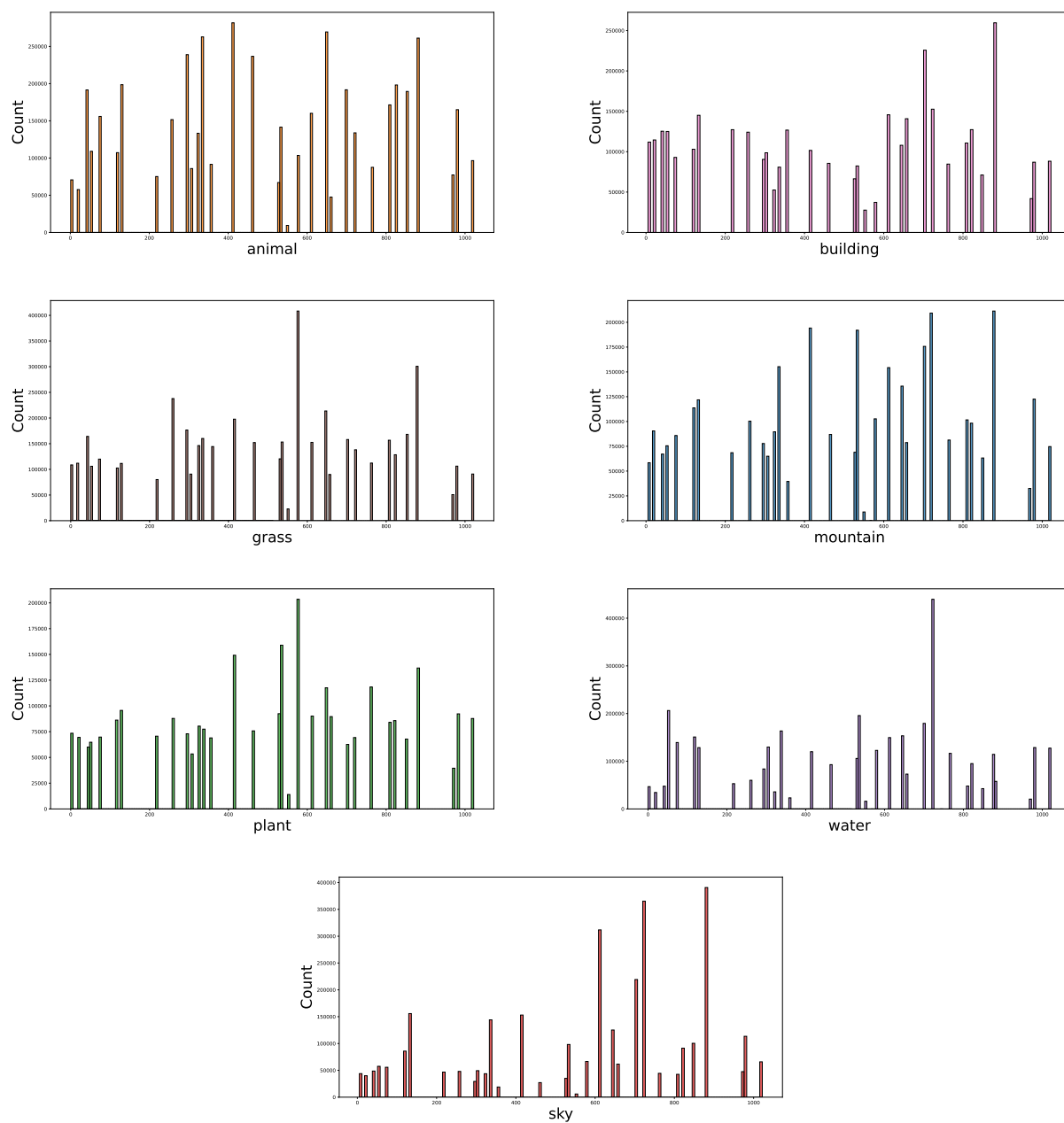


Figure 14: Code index distribution for 7 texture categories in OST dataset.

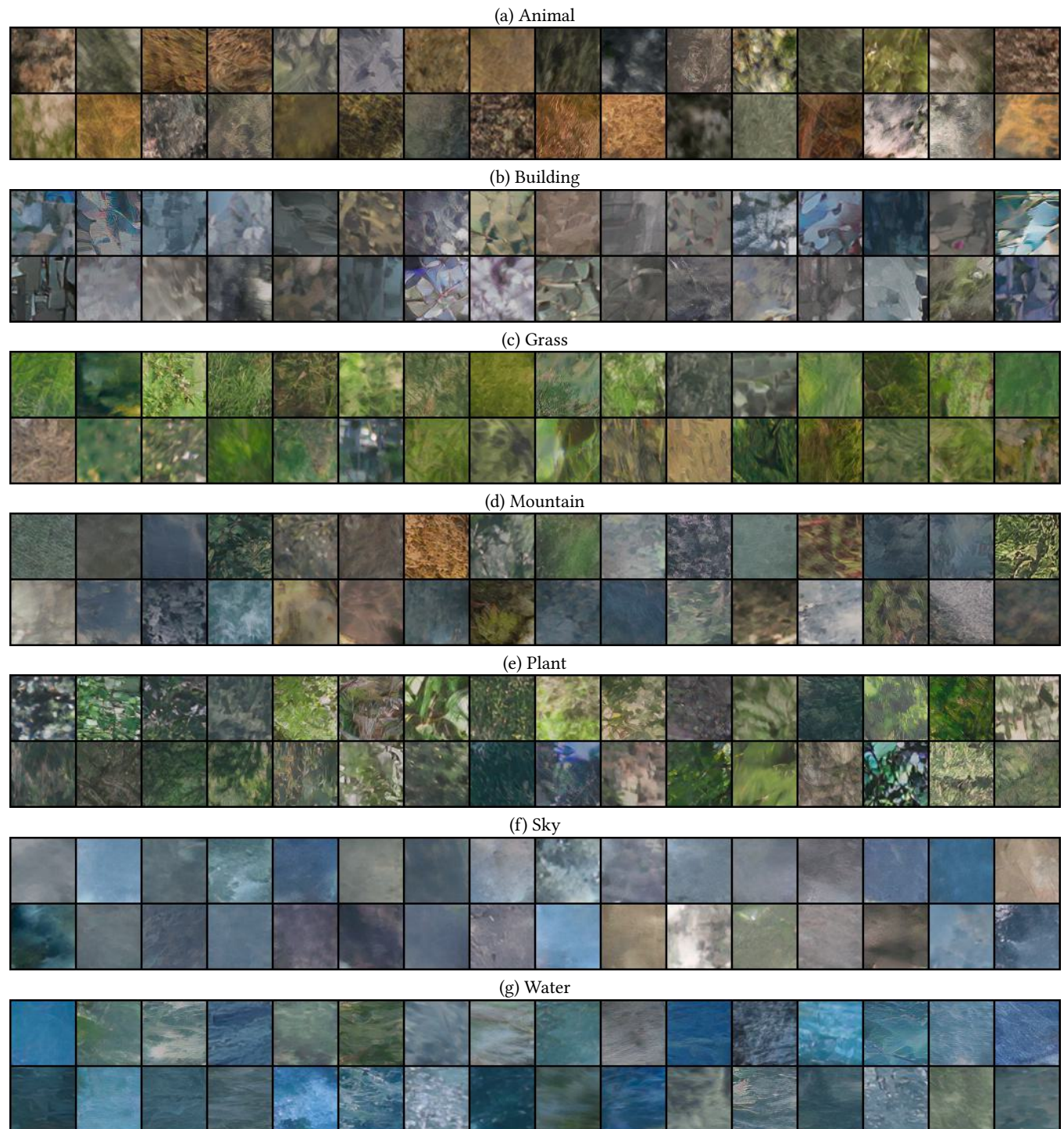


Figure 15: Visualization of different semantic-related textures encoded in HRP.

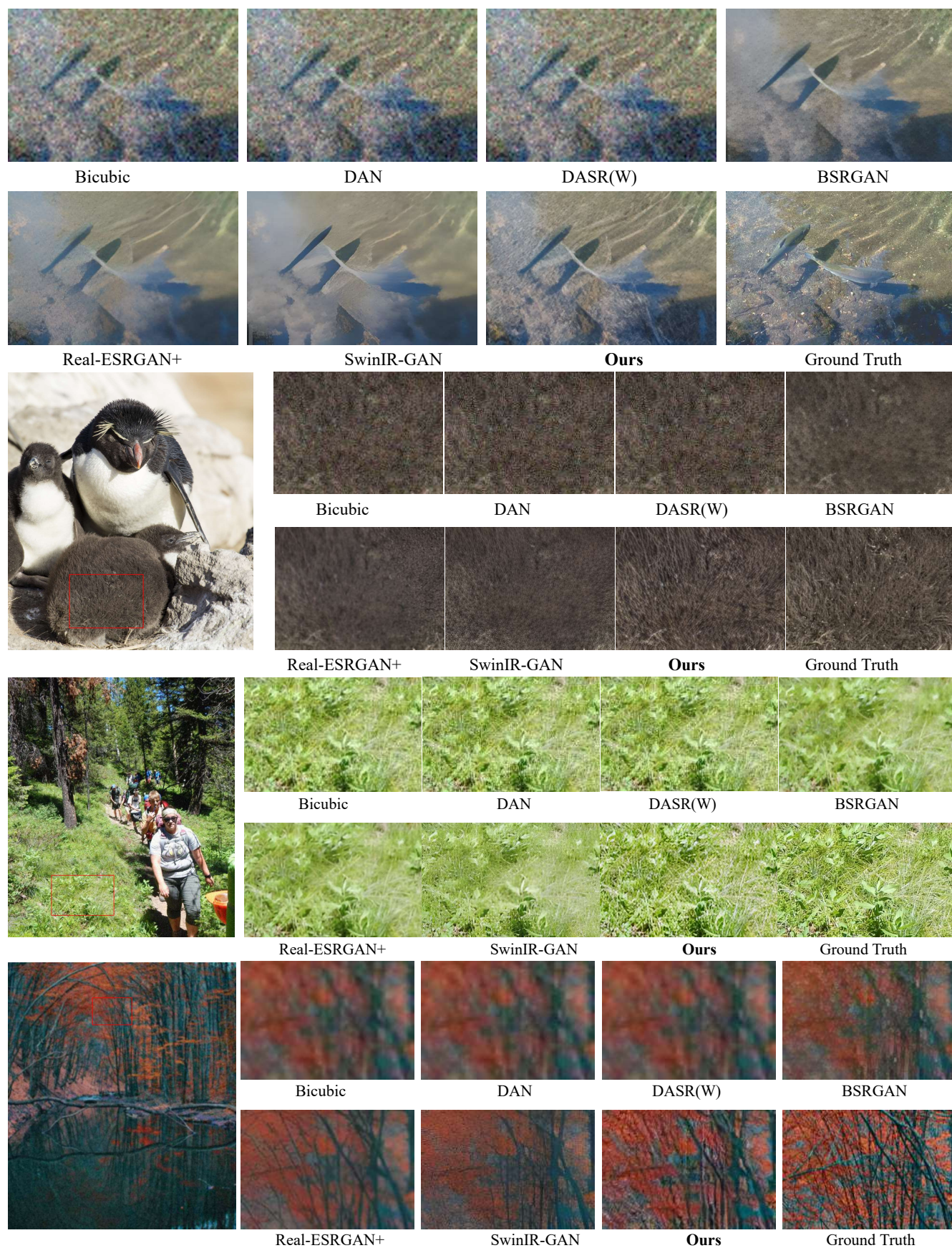


Figure 16: More results on synthetic benchmarks.

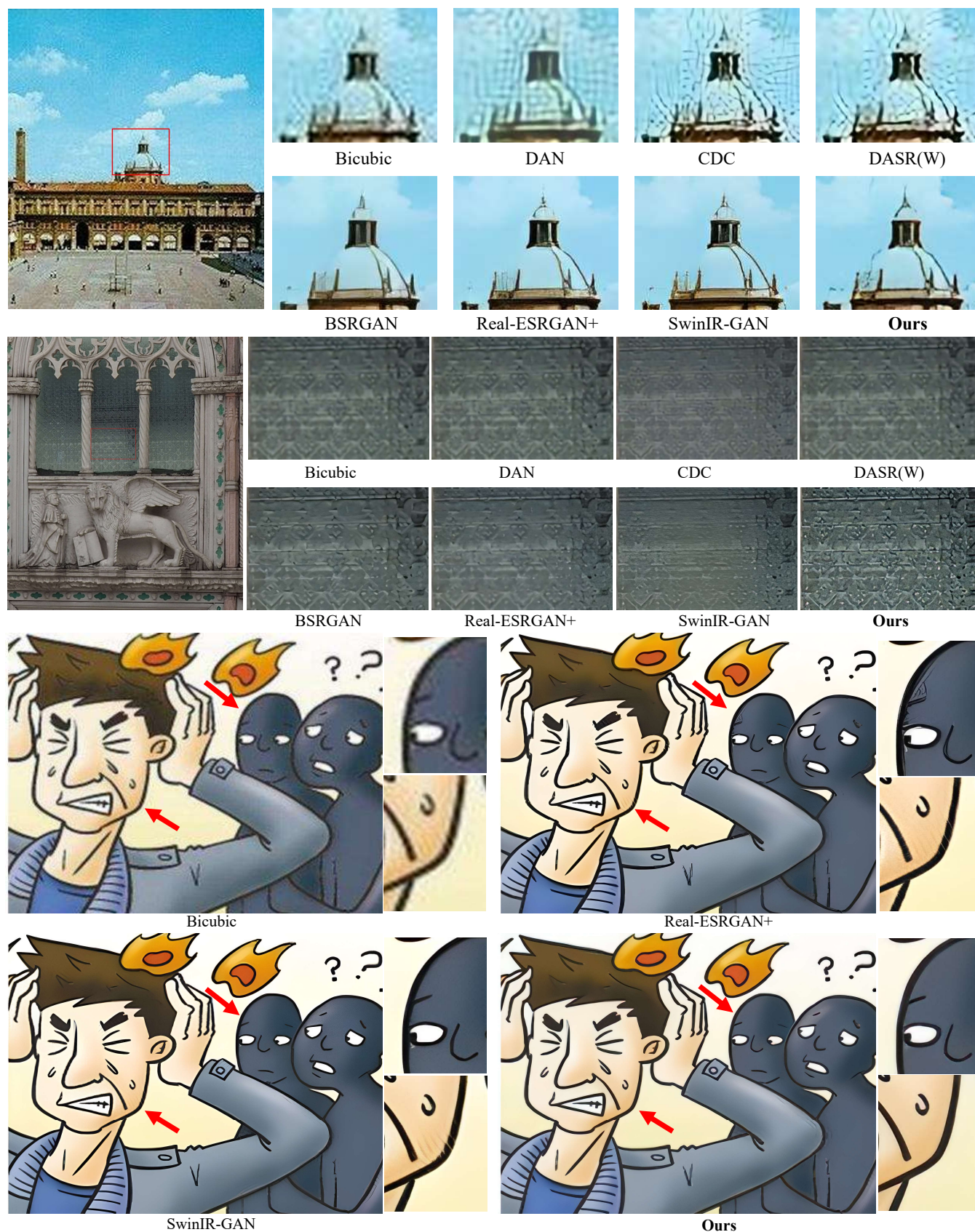


Figure 17: More results on real-world test images.